

Molecular Physics

An International Journal at the Interface Between Chemistry and Physics

ISSN: (Print) (Online) Journal homepage: <https://www.tandfonline.com/loi/tmph20>

Black-body radiation-induced photodissociation and population redistribution of weakly bound states in H_2^+

A. D. Ochoa Franco & M. Beyer

To cite this article: A. D. Ochoa Franco & M. Beyer (2022): Black-body radiation-induced photodissociation and population redistribution of weakly bound states in H_2^+ , Molecular Physics, DOI: [10.1080/00268976.2022.2133750](https://doi.org/10.1080/00268976.2022.2133750)

To link to this article: <https://doi.org/10.1080/00268976.2022.2133750>



© 2022 The Author(s). Published by Informa UK Limited, trading as Taylor & Francis Group



Published online: 27 Oct 2022.



Submit your article to this journal [↗](#)



Article views: 7



View related articles [↗](#)



View Crossmark data [↗](#)

Black-body radiation-induced photodissociation and population redistribution of weakly bound states in H_2^+

A. D. Ochoa Franco  and M. Beyer 

Department of Physics and Astronomy, LaserLaB, Vrije Universiteit Amsterdam, Amsterdam, Netherlands

ABSTRACT

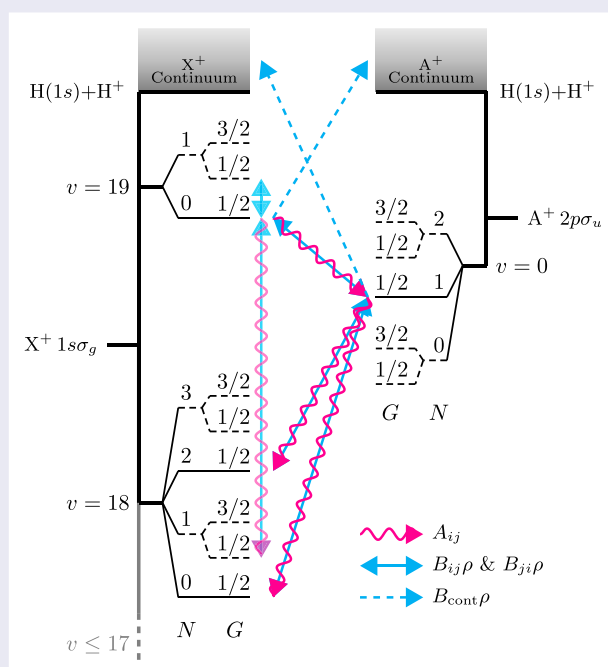
Molecular hydrogen ions in weakly bound states close to the first dissociation threshold are attractive quantum sensors for measuring the proton-to-electron mass ratio and hyperfine-induced ortho-para mixing. The experimental accuracy of previous spectroscopic studies relying on fast ion beams could be improved by using state-of-the-art ion trap setups. With the electric-dipole moment vanishing in H_2^+ and preventing fast spontaneous emission, radiative lifetimes of the order of weeks are found. We include the effect of black-body radiation that can lead to photodissociation and rovibronic state redistribution to obtain effective lifetimes for trapped ion experiments. Rate coefficients for bound-bound and bound-continuum processes were calculated using adiabatic nuclear wave functions and nonadiabatic energies, including relativistic and radiative corrections. Effective lifetimes for the weakly bound states were obtained by solving a rate equation model and lifetimes in the range of 4–523 and > 215 ms were found at room temperature and liquid nitrogen temperature, respectively. Black-body induced photodissociation was identified as the lifetime-limiting effect, which guarantees the purity of state-selectively generated molecular ion ensembles. The role of hyperfine-induced g/u -mixing, which allows pure rovibrational transitions, was found to be negligible.



ARTICLE HISTORY

Received 2 August 2022
Accepted 28 September 2022

KEYWORDS

Molecular ions;
photodissociation;
black-body radiation



CONTACT M. Beyer  m.beyer@vu.nl  Department of Physics and Astronomy, LaserLaB, Vrije Universiteit Amsterdam, De Boelelaan 1085, Amsterdam 1081 HV, Netherlands

© 2022 The Author(s). Published by Informa UK Limited, trading as Taylor & Francis Group
This is an Open Access article distributed under the terms of the Creative Commons Attribution-NonCommercial-NoDerivatives License (<http://creativecommons.org/licenses/by-nc-nd/4.0/>), which permits non-commercial re-use, distribution, and reproduction in any medium, provided the original work is properly cited, and is not altered, transformed, or built upon in any way.

1. Introduction

The hydrogen molecular ion (HMI) is the simplest molecular system and can be used to test quantum electrodynamics and to determine fundamental constants by comparing experimental and theoretical transition frequencies [1,2]. While *ab initio* theory reached a level of 10^{-11} relative accuracy for H_2^+ and HD^+ [3,4], a comparable experimental accuracy has only been achieved for the HD^+ isotopologue [1,2,5]. In these experiments, rovibrationally-cold HD^+ ions are held in a radio-frequency trap and sympathetically cooled to reach the Lamb-Dicke regime in order to suppress Doppler effects during the spectroscopic interrogation.

Cooling the rovibrational degrees of freedom of the hot HD^+ ions produced by electron bombardment relies on spontaneous emission; a process that is only possible in the heteronuclear isotopologues, because of the electric-dipole moment originating from the mass and charge asymmetry [6]. The absence of that very dipole moment for the homonuclear isotopologues has far-reaching consequences regarding the ion production, as well as the multitude of strong transitions available for spectroscopic studies: (i) with radiative lifetimes of the order of weeks [7], any rovibrational state distribution produced during electron bombardment will be conserved, drastically reducing the number of available ions participating in a single spectroscopic transition, and (ii) strong electric-dipole allowed transitions exist only between different electronic states.

Carrington and coworkers succeeded in measuring rovibronic transitions between weakly bound states of the ground ($X^+ \ ^2\Sigma_g^+$) and first excited ($A^+ \ ^2\Sigma_u^+$) electronic states of H_2^+ just below the $\text{H}(1s) + \text{H}^+$ dissociation threshold [8–12]. A fast ion beam with high current was used to compensate for the small number of ions per quantum state and having the transition frequencies in the microwave range helped limit the Doppler broadening. To avoid interaction broadening, the ion beam was directed through a sufficiently long microwave waveguide and the observation of forward and back-reflected modes allowed the cancellation of the first-order Doppler shifts. This resulted in an FWHM of 0.6 MHz and an absolute accuracy of the order of 0.5 MHz (relative accuracy 10^{-5}).

In a new generation of measurements, we aim at improving the accuracy of the transition frequencies between the weakly bound states, which have been found to show an enhanced sensitivity on the proton-to-electron mass ratio [13], by employing a similar ion trap setup as used in Ref. [2]. The suppression of Doppler-related effects and the careful control of magnetic fields

over a small trap volume have been shown to allow to reach Hertz-level accuracy [14].

This leaves the question of how to increase the population in individual quantum levels of the HMI, preferably creating the ions selectively in a single weakly bound rovibronic level. Such a state-selected ion generation can be achieved using mass-analysed threshold ionisation (MATI) [15]: this involves photoexcitation with a laser, slightly red-detuned from the targeted level in the ion $E^+(\nu', N')$, which will lead via direct ionisation and auto-ionisation to ions in lower lying states $E^+(\nu \neq \nu', N \neq N')$ as well as high- n Rydberg states converging to the $E^+(\nu', N')$ threshold. The *prompt* ions in unwanted states can be spatially separated from the neutral molecules in the Rydberg states, which are subsequently field-ionised to selectively provide ions in the state $E^+(\nu', N')$ for subsequent experiments [16].

In order to apply MATI for the efficient production of the weakly bound states in the vicinity of the dissociation threshold, a multi-step excitation pathway has to be employed to gradually increase the bond length from $\sim 1.4 a_0$ ($X(\nu = 0, N = 1)$) to $\sim 23.4 a_0$ ($X^+(\nu = 19, N = 1)$), as shown in the photoelectron spectroscopic studies by Beyer and Merkt for H_2 , HD and D_2 [17–19]. The crucial ingredient for the excitation of weakly bound ions, starting from the vibronic ground state of neutral molecular hydrogen, was the use of the long-range $\text{H}\bar{\text{H}}$ and $\text{B}\bar{\text{B}}$ intermediate states, first observed and characterised by W. Ubachs and his coworkers [20–22]. These states belong to the class of *ion-pair states* [23] and are characterised by large bond lengths and mixed electronic character (regarding the orbital-angular momentum ℓ in a single-centre description), allowing for the efficient generation of weakly bound molecular ions with $N = 0–10$.

Previous theoretical studies on the radiative lifetimes of the weakly bound states have shown lifetimes in excess of hundreds of seconds [7,24], even when including the effect of ortho-para or g/u -mixing due to the hyperfine structure [25], making them very attractive for precision measurements. However, neither of these studies addressed the effect of photodissociation and state redistribution induced by black-body radiation (BBR). The peak of the black-body spectrum (BBS) at room temperature is located at around 17 THz, overlapping with the electric-dipole spectrum of the weakly bound states and supporting the possibility of having a perceptible effect on the lifetimes and the state distribution of the selectively prepared ions.

In the following, we present a theoretical study on the effective lifetimes of HMI in weakly bound states, taking the effects of BBR and g/u -mixing into account.

Section 2 shows the calculation of the Einstein coefficients for bound-bound and bound-continuum transitions, required to solve the rate equations for the HMI. Effective lifetimes and the time evolution of the state distributions are shown in Section 3 and in Section 4 the results are discussed in view of the planned precision measurements mentioned above.

2. Theory

2.1. Level structure

In this study, we consider electric-dipole transitions between rovibrational levels of the electronic ground and excited state $X^+ {}^2\Sigma_g^+$ and $A^+ {}^2\Sigma_u^+$, respectively. To determine the transition strengths, the vibrational wave functions are obtained by solving the nuclear Schrödinger equation

$$\left[-\frac{1}{2\mu} \frac{d^2}{dR^2} + \frac{N(N+1)}{2\mu R^2} + U(R) - E_{vN} \right] \psi_{vN}(R) = 0, \quad (1)$$

where μ is the nuclear-reduced mass and R is the internuclear distance. $U(R)$ is the Born-Oppenheimer (BO) potential energy curve with the adiabatic correction added and was taken from Ref. [26]. Atomic units and the values of the fundamental constants from 2018 CODATA [27] were used. The integration is performed using the renormalised Numerov method [28] with a radial step size of $0.01a_0$, resulting in dissociation energies in agreement with the ones given in Ref. [24]. Small deviations below 1 cm^{-1} originate from disregarding nonadiabatic, relativistic and QED effects in the current calculation, which tend to vanish for the dissociation energies of the weakly bound states, as the molecular corrections approach the atomic values. The rate coefficients in Section 2.3 are obtained using the adiabatic nuclear wave functions, but employing the exact nonadiabatic energies (including relativistic and radiative corrections) from Ref. [24].

The $X^+ {}^2\Sigma_g^+$ state has 19 vibrational states with at least 4 rotational levels, $0 \leq N \leq 3$, and $v = 19$, which has only 2 rotational levels, $N = 0$ and $N = 1$. The repulsive $A^+ {}^2\Sigma_u^+$ state supports one vibrational state, $v = 0$, with three rotational levels, $0 \leq N \leq 2$. A $v = 1$ halo state exists when the hyperfine structure is neglected [18,29] but was disregarded in the current work because of an insignificant Franck-Condon overlap. The relevant weakly bound states are depicted in the energy-level diagram in Figure 1, where it can be seen that the X^+ ($v = 19, N = 0, 1$) levels lie above the A^+ ($v = 0$) manifold, allowing for spontaneous emission. Rovibrational states of X^+ with $13 \leq v \leq 19$ and $0 \leq N \leq 3$ are considered,

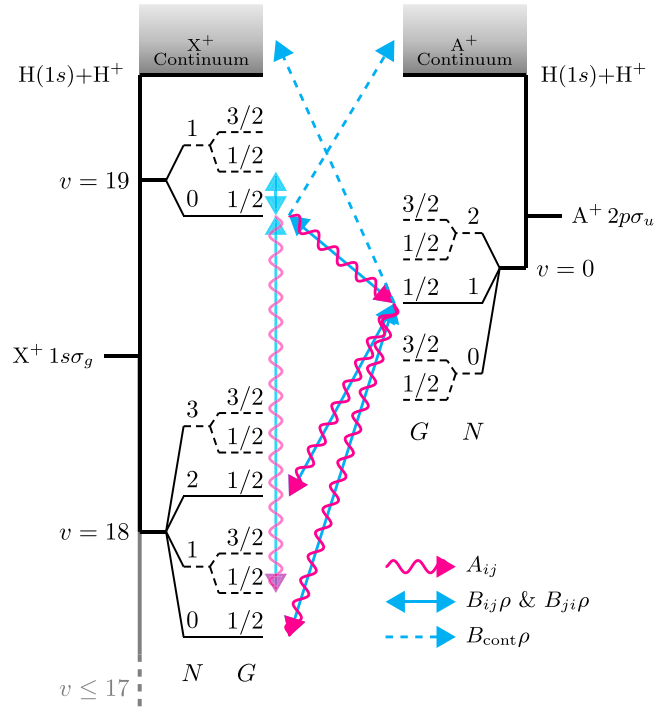


Figure 1. Energy-level diagram of the weakly bound states of H_2^+ . The ground electronic state, $X^+ {}^2\Sigma_g^+$, is depicted on the left-hand side, displaying the dissociation continuum on the top and the two highest vibrational levels. Levels with $v = 13-17$ are not shown for clarity but are taken into account in the calculation. On the right-hand side, the first excited electronic state, $A^+ {}^2\Sigma_u^+$, is shown with a single vibrational level, $v = 0$, and the dissociation continuum. For both electronic states, the rotational levels denoted with a dashed line are the ortho-levels with $l = 1$. The arrows represent a simplified version of the transitions present for para- H_2^+ with the whole population starting in the X^+ ($v = 19, N = 0, G = 1/2$) level; wavy red lines indicate spontaneous emission, the double-headed solid blue lines show stimulated emission and absorption, and the single-headed dashed blue line stands for absorption into the continuum (all states experience absorption into the continuum, but only a few are explicitly shown). The forbidden transitions, allowed by g/u -mixing, are also shown. Neglecting spin-rotation interactions, the levels F are degenerate and not shown.

with the range of v based on the value of the Franck-Condon factor, which rapidly decreases from ~ 0.5 for $A^+ - X^+$ ($v = 19$) to $\sim 10^{-8}$ for $A^+ - X^+$ ($v = 13$).

The dissociation continua of the X^+ and A^+ state, indicated as a shaded area at the top of Figure 1, play a crucial role in the present calculation. The continuum wave functions are obtained using outward integration of Equation (1) and are energy normalised by scaling their amplitude to $\sqrt{(2\mu/\pi k)}$ with $k = \sqrt{(2\mu(\epsilon - U(\infty)))}$, and ϵ being the kinetic energy of the continuum state [30]. The energy-normalised continuum wave functions have dimensions of $[(\text{Length Energy})^{-1/2}]$. To adequately account for the photodissociation of the X^+ ($v = 2$) and

$X^+(v, 3)$ states, the continuum of A^+ is taken into account with $N \leq 4$.

The hyperfine structure of the rovibrational levels in H_2^+ is described using Hund's case $b_{\beta S}$ with the coupling scheme:

$$\begin{aligned} \mathbf{I} &= \mathbf{I}_1 + \mathbf{I}_2, \\ \mathbf{G} &= \mathbf{S} + \mathbf{I}, \\ \mathbf{F} &= \mathbf{G} + \mathbf{N}. \end{aligned}$$

The coupling of \mathbf{S} and \mathbf{I} to form \mathbf{G} is caused by the Fermi contact interaction,

$$H_F = b_F(v, N) \mathbf{S}^{(1)} \cdot \mathbf{I}^{(1)}, \quad (2)$$

which is the leading term in the hyperfine Hamiltonian with $b_F(v, N)$ of the order of ~ 700 MHz. The coupling constants were computed using the adiabatic nuclear wave functions and the electron densities from Ref. [18] (see Tables A1 and A2 in Appendix 1). For $X^+(19, 1)$ we find excellent agreement with the experimentally determined value from Ref. [10].

The two nuclear-spin modifications para, with $I = 0$, and ortho, with $I = 1$, combine with even (odd) and odd (even) rotational levels of the $X^+ {}^2\Sigma_g^+ (A^+ {}^2\Sigma_u^+)$ state, respectively, as imposed by the Pauli principle. The rotational levels of ortho- H_2^+ are indicated using dashed lines in Figure 1. The Fermi contact interaction in Equation (2) splits each rotational level in ortho- H_2^+ in a $G = 1/2$ and $G = 3/2$ component, whereas no splitting appears for para- H_2^+ with $G = S = 1/2$. The couplings of the electron and nuclear spins to the molecular rotation are weak and were neglected, which leads to a degeneracy of all F components for a given (N, G) pair.

Close to the dissociation limit, the hyperfine interaction becomes comparable to the splitting of the *gerade* and *ungerade* electronic states, which leads to g/u -mixing (or ortho-para mixing) of levels with $G = 1/2$ and the same value of N [31].

2.2. Line strengths

To calculate the population redistribution induced by BBR, we evaluate the line strength for the electric-dipole transition from lower state $|\eta\Lambda; v; NSIGF\rangle$ to upper state $|\eta'\Lambda'; (v'/\epsilon); N'SIG'F'\rangle$, defined as [32]

$$\begin{aligned} S_{\eta', v', F'; \eta, v, F} &= \sum_{MM'} |\langle \eta'\Lambda'; (v'/\epsilon); \\ &\quad N'G'F'M' | \boldsymbol{\mu}_e^{(1)} | \eta\Lambda; v; NGFM \rangle|^2 \\ &= \mathcal{S}_{\Lambda'N'G'F', \Lambda NGF} \\ &\quad \times |\langle \eta'\Lambda'; (v'/\epsilon)N' | \boldsymbol{\mu}_{e,q}^{(1)} | \eta\Lambda; vN \rangle|^2, \quad (3) \end{aligned}$$

which was expressed in a rotational and vibronic part in the second line, with the electric-dipole transition moment $\boldsymbol{\mu}_e^{(1)}$. The quantum numbers v' or ϵ indicate if the upper state is bound or a continuum state. For clarity, the quantum numbers $S = 1/2$ and $I = 0, 1$ are not explicitly written and the vibrational quantum number v is replaced with ϵ for continuum states. After transforming to the molecular-fixed coordinate system, the rotational integral can be obtained by making use of the following matrix element [33,34]

$$\begin{aligned} &|\langle \Lambda'N'G'F'M' | \mathbf{D}_{pq}^{(1)*} | \Lambda NGFM \rangle|^2 \\ &= \delta_{GG'}(2F+1)(2F'+1)(2N+1)(2N'+1) \\ &\quad \times \begin{pmatrix} N' & 1 & N \\ -\Lambda' & q & \Lambda \end{pmatrix}^2 \begin{Bmatrix} N' & F' & G \\ F & N & 1 \end{Bmatrix}^2 \\ &\quad \times \begin{pmatrix} F' & 1 & F \\ -M' & p & M \end{pmatrix}^2. \quad (4) \end{aligned}$$

For $\Sigma - \Sigma$ transitions, $q = 0$, and these matrix elements vanish unless $\Delta G = 0$ and $\Delta N = \pm 1$. For isotropic excitation (BBR is unpolarised) and emission, Equation (4) is summed over p, M and M' , and the Hönl-London factor $\mathcal{S}_{\Lambda'N'G'F', \Lambda NGF}$ including hyperfine structure is obtained as:

$$\begin{aligned} \mathcal{S}_{\Lambda'N'G'F', \Lambda NGF} &= \delta_{GG'}(2F+1)(2F'+1)(2N+1)(2N'+1) \\ &\quad \times \begin{pmatrix} N' & 1 & N \\ -\Lambda' & q & \Lambda \end{pmatrix}^2 \begin{Bmatrix} N' & F' & G \\ F & N & 1 \end{Bmatrix}^2. \quad (5) \end{aligned}$$

In the following, the Hönl-London factor for a rotational line without and with spin is considered.

Neglecting spin, with $(S = 0, I = 0) \rightarrow G = 0$ and $F = N$, Equation (5) simplifies to the more common expression

$$\mathcal{S}_{\Lambda'N', \Lambda N} = (2N+1)(2N'+1) \begin{pmatrix} N' & 1 & N \\ -\Lambda' & q & \Lambda \end{pmatrix}^2. \quad (6)$$

For the general case in Equation (5), we establish the sum rule

$$\begin{aligned} \mathcal{S}_{\Lambda'N'G, \Lambda NG} &\equiv \sum_{FF'} \mathcal{S}_{\Lambda'N'GF', \Lambda NGF} \\ &= (2G+1) \mathcal{S}_{\Lambda'N', \Lambda N}, \quad (7) \end{aligned}$$

using the orthogonality of the 6- j symbols [34,35]. Notice, that the right-hand side of this equation depends on spin only through the factor of $(2G+1)$. When $I = 0$,

$(2G + 1) \rightarrow (2S + 1)$, and the spin-independent Hönl-London factor is recovered, multiplied with the electron spin degeneracy factor $(2S + 1)$ [35,36].

The vibronic matrix elements of $\mu_{e,q}^{(1)}$ were calculated using the adiabatic nuclear wave functions from Equation (1) and the electric-dipole transition moment, $\mu_{X^+-A^+}(R)$ from Ref. [26]. For bound-bound transitions we have

$$\begin{aligned} \mu_{v'N',vN} &\equiv \langle A^+, v'N' | \mu_{e,0}^{(1)} | X^+, vN \rangle \\ &= \int dR \psi_{A^+v'N'} \mu_{X^+-A^+} \psi_{X^+vN}, \end{aligned} \quad (8)$$

and the transition moments for pure rovibrational transitions due to g/u -mixing were taken from Ref. [25].

For bound-continuum transitions to a dissociative state with kinetic energy ϵ , for instance, $X^+(v, N) - A^+(\epsilon, N')$, the matrix elements of $\mu_{e,q}^{(1)}$ are given by

$$\begin{aligned} \mu_{N',vN}(E_\gamma) &\equiv \langle A^+, \epsilon N' | \mu_{e,0}^{(1)} | X^+, vN \rangle \\ &= \int dR \psi_{A^+\epsilon N'} \mu_{X^+-A^+} \psi_{X^+vN}, \end{aligned} \quad (9)$$

where $\mu_{N',vN}(E_\gamma)$ are continuous functions of the photon energy,

$$E_\gamma = \epsilon - E_{vN}, \quad (10)$$

and $E_{vN} < 0$ is the binding energy of the bound state. Notice that since the continuum wave functions are energy-normalised, this transition moment has units of $(ea_0)/E_H^{1/2}$.

Finally, Equation (3) can be written for our specific case as

$$S_{\eta'v'N'G, \eta vNG} = (2G + 1) \mathcal{S}_{N',N} |\mu_{\eta'v'N', \eta vN}|^2. \quad (11)$$

The photodissociation cross-section (PDCS) in atomic units (a_0^2) is given by [10,36]

$$\sigma_{\eta vN}(E_\gamma) = \frac{4}{3} \pi^2 \sum_{N'} \alpha E_\gamma \frac{\mathcal{S}_{N',N} |\mu_{N',vN}(E_\gamma)|^2}{(2N + 1)}, \quad (12)$$

and is obtained by summing over all (F, F') and N' . Using Equation (7), the total state degeneracy factor $(2F + 1)$ in the denominator simplifies to $(2N + 1)$.

2.3. Einstein coefficients and rate equations

To determine the time evolution of an ion ensemble prepared in a single initial state, we solve the rate equations

of the form

$$\begin{aligned} \frac{dN_j(t)}{dt} &= \sum_{i>j} A_{ji} N_i(t) - \sum_{i<j} A_{ij} N_j(t) \\ &+ \sum_{i \neq j} \bar{B}_{ji} N_i(t) - \sum_{i \neq j} \bar{B}_{ij} N_j(t) - \bar{B}_{\text{cont},j} N_j(t), \end{aligned} \quad (13)$$

where the notation has been shortened, where appropriate, such that the indices i and j stand for any state $|\eta vN\rangle$, N_j is the number of ions in the state j , A_{ij} is the rate of spontaneous emission for the transition $j \rightarrow i$, \bar{B}_{ij} is the rate of stimulated emission, \bar{B}_{ji} is the rate of absorption, and \bar{B}_{cont} is the rate of absorption to the continuum.

The rate of spontaneous emission in atomic units (E_H/\hbar) is given by

$$A_{ij} = \frac{4}{3} (\alpha E_\gamma)^3 \frac{S_{ij}}{g_j}, \quad (14)$$

where g_j is the degeneracy of the initial state. It can be shown that this equation determines the decay rate of, both, a rotational line without spin using the Hönl-London factor from Equation (6) with $g_j = 2N + 1$, and a hyperfine level F using Equation (4) with $g_j = 2F + 1$ [37]. However, to obtain the decay rate for a rotational line with spin it is necessary to sum over the fine or hyperfine structure levels F and F' [32,37,38], that is,

$$\begin{aligned} A_{v'N',vN} &= \frac{\sum_{FF'} A_{v'N'GF',vNGF}}{\sum_F (2F + 1)} \\ &= \frac{\sum_{FF'} \mathcal{S}_{\Lambda'N'GF',\Lambda NGF} |\mu_{v'N',vN}|^2}{\sum_F (2F + 1)}, \end{aligned} \quad (15)$$

where $\sum_F (2F + 1) = (2G + 1)(2N + 1)$ [35]. This can be simplified to

$$A_{v'N',vN} = \frac{4}{3} (\alpha E_\gamma)^3 \frac{\mathcal{S}_{N',N}}{(2N + 1)} |\mu_{v'N',vN}|^2. \quad (16)$$

Similar to the PDCS the dependence on G cancels out so that different hyperfine levels G from a rovibrational state (vN) decay at the same rate to another state $(v'N')$. The combination of Hönl-London factor and initial state degeneracy in Equation (14) for different cases can be

summarised as follows:

$$\mathcal{S}_{ij} = \begin{cases} \text{Equation (6)} \\ \text{Equation (7), } G \rightarrow S \\ \text{Equation (7)} \\ \text{Equation (5)} \\ \text{Equation (4)} \end{cases}$$

$$g_j = \begin{cases} (2N+1) \\ (2N+1)(2S+1) \\ (2N+1)(2G+1), \\ (2F+1) \\ 1 \end{cases} \quad (17)$$

where the first line is for a spin-less rotational line, the second line is for a rotational line with electronic spin and $I = 0$, the third line is for a rotational line with nuclear spin, the fourth line is for a hyperfine level F , and the last line is for a Zeeman component of the hyperfine structure.

The rate of stimulated emission \bar{B}_{ij} in Equation (13) has the same units as A_{ij} and is related to the Einstein B_{ij} coefficient through the photon density, $\rho(T, E_\gamma)$, that is,

$$\bar{B}_{ij} \equiv B_{ij} \rho(T, E_\gamma), \quad (18)$$

where B_{ij} is given in atomic units $a_0^3 E_H / \hbar$ by

$$B_{ij} = \frac{4}{3} \pi^2 \frac{\mathcal{S}_{ij}}{g_j} \quad \text{and} \quad (19)$$

$$\rho(T, E_\gamma) = \frac{1}{\pi^2} (\alpha E_\gamma)^3 \frac{1}{\exp(E_\gamma / k_B T) - 1}, \quad (20)$$

with atomic units $1/a_0^3$.

For absorption, the rate coefficient is expressed as

$$B_{ji} = (g_j/g_i) B_{ij}. \quad (21)$$

The rate of absorption to the continuum – or photodissociation rate –, \bar{B}_{cont} , was calculated using Equation (18) and Equation (19) considering the E_γ -dependent electric-dipole moment, as in Equation (12). Then, we integrated with respect to E_γ and summed over the possible N' values in the continuum, to obtain

$$\bar{B}_{\text{cont}, \eta \nu N} = \frac{4}{3} \pi^2 \sum_{N'} \int dE_\gamma \frac{\mathcal{S}_{N', N} |\mu_{e, \eta \nu N N'}(E_\gamma)|^2}{(2N+1)} \rho(T, E_\gamma). \quad (22)$$

This equation is equivalent to the photodissociation rate [39], $\Gamma_{\text{PD}} = \int dE_\gamma \sigma(E_\gamma) I(T, E_\gamma) / E_\gamma$, where I is

the radiation intensity distribution. Numerical integration of this equation is performed using Gauss-Legendre quadrature with 4000 energy steps in the range $0 < E_\gamma < 0.035 E_H$.

3. Results

Figure 2(a) displays the $A^+ - X^+$ stick spectrum with the line strengths according to Equation (11), which agree with those of Ref. [40] within 0.03%. The transitions appear grouped in vibrational bands and spread over a frequency range from 14 GHz to 62 THz. In the low-frequency region, the transitions involving the two highest vibrational levels of the ground state ($\nu = 18, 19$) exhibit the largest line strengths, up to $338 e^2 a_0^2$. This is caused by the favourable Franck-Condon factors and the large transition dipole moment (proportional to the internuclear distance), which is characteristic of charge-transfer transitions [41]. It can be noticed, that the spacing between individual rotational lines and vibrational bands becomes comparable when approaching the dissociation threshold, indicating the breakdown of the BO approximation and a reversal of the typical hierarchy of motion.

The dashed lines in Figure 2(a) indicate the transitions, which appear because of intensity borrowing due to the g/u -mixing. The strongest additional line is attributed to the purely rotational $X(19,0)-(19,1)$ transition, which was experimentally observed by Critchley and coworkers [42].

The PDCS for $X^+(\nu = 13 - 19, N = 1)$ and $A^+(\nu = 0, N = 1)$ as obtained from Equation (12) is shown in Figure 2(b). For clarity, we omitted the PDCS of the levels with $N \neq 1$, which shows a similar shape. The largest N -dependence of the PDCS is expected for $X^+(19)$ and can be seen to be of the order of $1 a_0^2$, by comparing the curves for $X^+(19,0)$ and $X^+(19,1)$. For lower vibrational states, the difference in the PDCS vanishes – in accordance with the BO approximation. Three relevant characteristics of the PDCS can be noticed: (i) A threshold appears, located at the dissociation energy of the rovibrational level, which increases with decreasing ν , (ii) They possess a global maximum close to their threshold, and (iii) Successive local maxima decrease in amplitude.

Employing Equation (20), Figure 2(c) illustrates the BBS photon density at room temperature (293 K) and at liquid nitrogen temperature (77 K), with maxima at 17 and 4 THz, respectively. A comparison of Figure 2(a–c) clearly exemplifies the importance of BBR induced processes for bound-bound and bound-continuum transitions involving the weakly bound states, with the BBS peak overlapping with the maximum of the PDCS of the levels $X^+(\nu = 16 - 17)$.

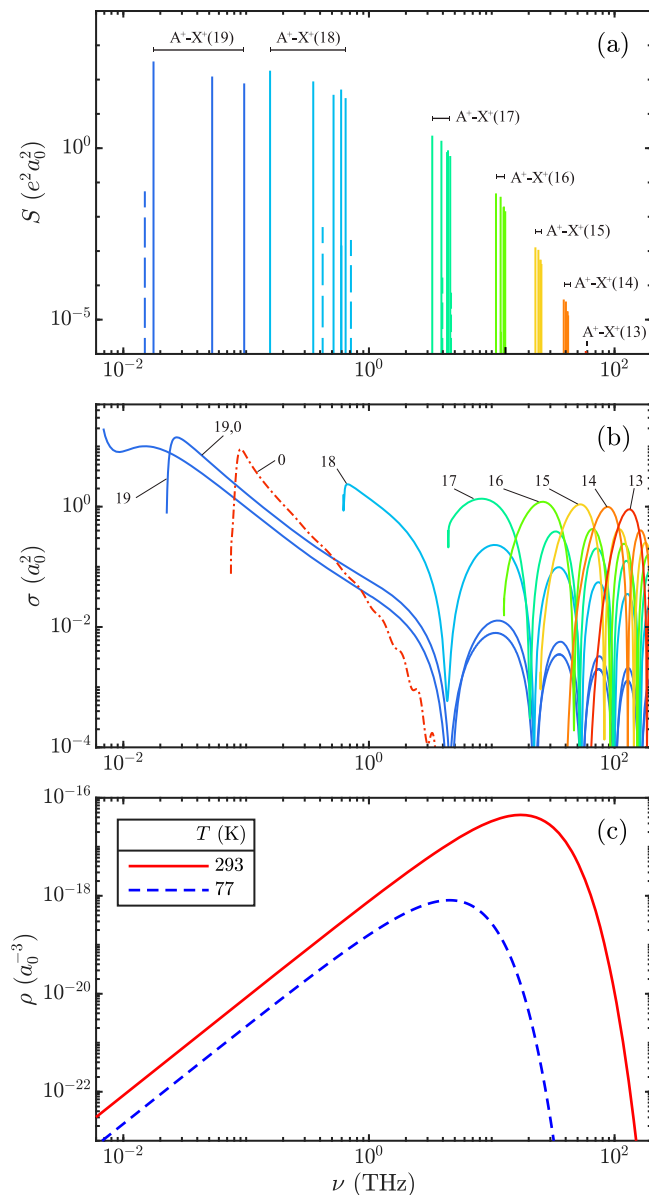


Figure 2. (a) Bound-bound $A^+ - X^+$ stick spectrum of H_2^+ , with the labels indicating the vibrational bands. The forbidden transitions (allowed by g/u -mixing) are indicated as dashed lines. (b) Photodissociation cross-section for $X^+(v = 13 - 19, N = 1)$ (solid line) and $A^+(v = 0, N = 1)$ (dash-dotted line). For comparison, $X^+(19, 0)$ is also shown. (c) Black-body photon density at room (solid line) and at liquid nitrogen (dashed line) temperature. See text for details.

To study the time evolution of the ion's rovibronic state distribution under the influence of BBR, the rate equations in Equation (13) were solved for different initial conditions, corresponding to having all ions in a single rovibronic state.

Figure 3 and Figure 4 display the internal state distributions as a function of time, with the population being initially in the $X^+(19, 0)$ and $X^+(19, 1)$ state at

293 and 77 K, respectively. The possible excitation and decay pathways for ions initially in the $X^+(19, 0)$ state are indicated in Figure 1, where $X^+(v \leq 17)$ states are not shown for clarity but are connected in the same way as $X^+(18)$. Solving the corresponding rate equations for $T = 293$ K leads to the normalised populations as shown in Figure 3(a). As dictated by the electric-dipole selection rules, the $X^+(19, 0)$ population can only be transferred to the $A^+(0, 1)$ bound state, or into the A^+ dissociation continuum, with the latter process being much more efficient. Subsequently, the $A^+(0, 1)$ state is transferred to the lower lying $X^+(v \leq 18)$ levels via spontaneous and stimulated emission. Whereas stimulated emission is dominant at 293 K for transitions down to $X^+(17, 2)$, spontaneous emission becomes the dominant process for the population of the level $X^+(17, 0)$ and below. Numerical values of the rate coefficients can be found in Tables A3–A7 in Appendix 2. After a few hundred milliseconds, the population of the initially unpopulated bound states reaches a maximum, before ultimately approaching zero because of BBR-induced photodissociation. A noteworthy exception are X^+ states with $v \leq 16$, approximately 0.001% of the initial population, which are trapped because the BBR does not provide enough photon flux at these high frequencies.

All states populated during the decay of $X^+(19, 0)$ are para- H_2^+ states with $G = 1/2$, unless the g/u -mixing is taken into account. The mixing of gerade and ungerade levels allows pure rovibrational transitions, which were included in the rate equations, and the results are shown in Figure 3(b) for $X^+(19, 0, 1/2)$, where it can be seen that also ortho- H_2^+ states attain non zero population (only the $G = 1/2$ component, as we have $\Delta G = 0$). The forbidden transitions lead to population in $X^+(17, 1)$, $X^+(18, 1)$, and $X^+(19, 1)$, and eventually through absorption and emission via the $A^+(0, 0/2)$ states also to some population in $X^+(18, 3)$ and $X^+(17, 3)$. Despite the effect of the g/u -mixing, the decay of the initial state is not significantly affected, because the line strengths of the forbidden transitions are too small to compete with direct photodissociation. The maximum population in the intermediately populated ortho-states remains two orders of magnitude smaller than the maximum population acquired by the intermediate para-states.

Figure 3(c,d) considers the state redistribution with and without g/u -mixing starting in the $X^+(19, 1)$ level. The overall behaviour is similar to the one discussed for $X^+(19, 0)$, with the main difference that the initial state with $N = 1$ has now two bound states to transfer to, $A^+(0, 0)$ and $A^+(0, 2)$. It can be seen that the states $X^+(18, 1)$ and $X^+(17, 1)$ attain a larger population than

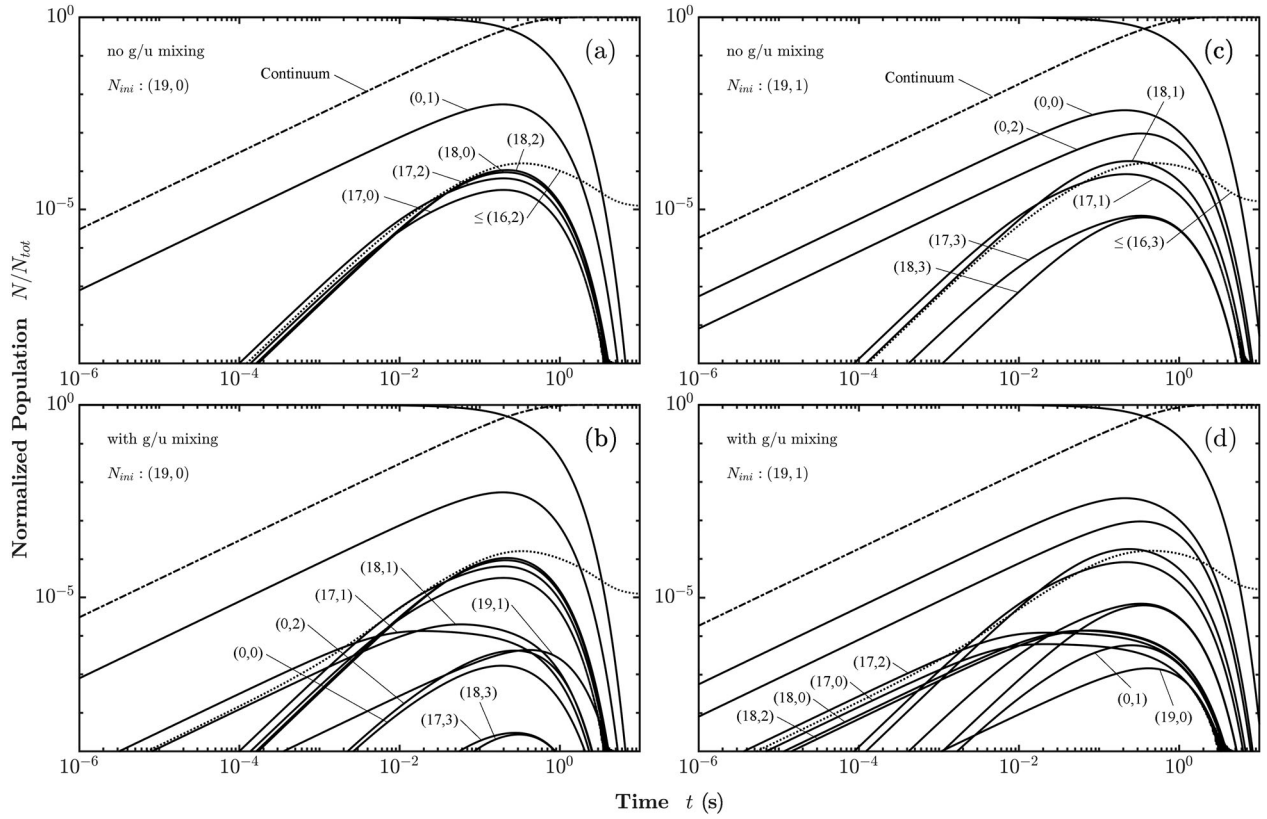


Figure 3. Time evolution of the rovibronic state populations at 293 K with the ions selectively prepared in: (a) Para- X^+ (19, 0) with no g/u -mixing. (b) Para- X^+ (19, 0) including g/u -mixing. Labels are added to the now-accessible ortho-states and the repeated labels from panel (a) are omitted. (c) Ortho- X^+ (19, 1) without g/u -mixing. (d) Ortho- X^+ (19, 1) with g/u -mixing.

the states X^+ (18, 3) and X^+ (17, 3), as the latter states can be only reached from level A^+ (0, 2).

The rovibronic state evolution at 77 K is presented in Figure 4. Most results are qualitatively the same as for room temperature; however, two main differences can be identified: (i) Photodissociation rates are reduced compared to room temperature so that the bound-bound redistribution becomes more important and intermediate levels reach around 3% of the initial population. (ii) The vibrational state with the largest acquired population is X^+ (17) instead of X^+ (18). This is because the population transfer between A^+ (0) and X^+ (18) at 293 K is mainly driven by stimulated emission. However, at 77 K, this rate of stimulated emission is about 33% lower and the redistribution is mostly driven by spontaneous emission, which favours population transfer to the X^+ (17) level.

The lifetime of a quantum state can be calculated from the spontaneous emission rate as

$$1/\tau_j = \sum_i A_{ij}. \quad (23)$$

In the presence of resonant radiation, an effective lifetime can be defined that also takes into account

stimulated emission and absorption [43]:

$$1/\tau_{\text{eff},j} = \sum_i [A_{ij} + \bar{B}_{ij}] + \bar{B}_{\text{cont},j}. \quad (24)$$

These effective lifetimes were calculated for all weakly bound states by solving the rate equations and determining the time at which the normalised population of the initial state reached $1/e$. Estimation of the effective lifetimes was obtained using Equation (24) and was found to agree with the numerical results within 3%. The results for 293 and 77 K are presented in Tables 1 and 2, respectively, and are displayed in Figure 5. The following observations can be made: (i) At 293 K, the lifetimes range from 4 ms for X^+ (17, 0) to 523 ms for X^+ (19, 1), whereas at 77 K, they range from 216 ms for X^+ (17, 0) – two orders of magnitude more – to 1 min for X^+ (16, 0) or days for X^+ (15, 0). (ii) The lifetimes of the various rotational levels for a particular vibrational state are very similar. (iii) The lifetimes of the A^+ states are not significantly affected by the change in temperature. (iv) The effect of the g/u -mixing is insignificant.

It should be noticed that for states with $\bar{B}_{\text{cont}} \gg \bar{B} \sim A$, the effective lifetime from Equation (24) becomes

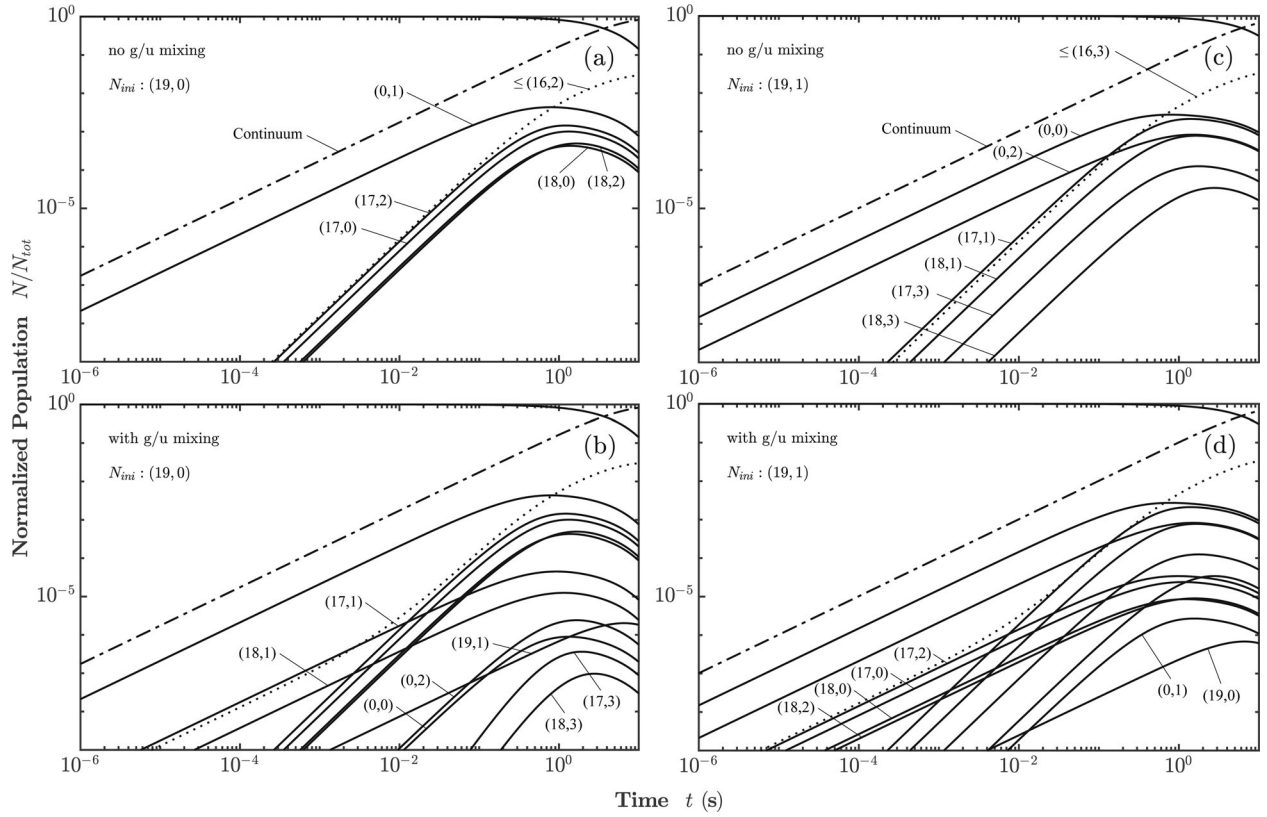


Figure 4. Time evolution of the rovibronic state populations at 77 K with the ions selectively prepared in: (a) Para- X^+ (19,0) with no g/u -mixing. (b) Para- X^+ (19,0) including g/u -mixing. Labels are added to the now-accessible ortho-states and the repeated labels from panel (a) are omitted. (c) Ortho- X^+ (19,1) without g/u -mixing. (d) Ortho- X^+ (19,1) with g/u -mixing.

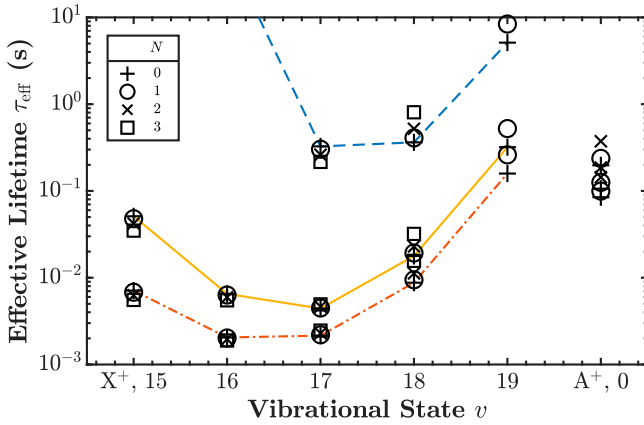


Figure 5. Effective lifetimes of the weakly bound states of H_2^+ . A line is drawn connecting states with $N = 0$; dashed blue line for 77 K, solid orange line for 293 K and dash-dotted red line for 400 K.

$\tau_{\text{eff}} \approx 1/\bar{B}_{\text{cont}}$, so absorption to the continuum is the determining factor for the lifetime.

To estimate the error in the rate constants and the calculated effective lifetimes, we determine the sensitivity of A and τ_{eff} regarding the following approximations: (i) Using BO vibrational wave functions and energies results in a change of $\Delta A/A = 0.0253$ and $\Delta \tau_{\text{eff}}/\tau_{\text{eff}} = 0.0191$.

Table 1. Effective lifetimes of the weakly bound states of H_2^+ at 293 K. Level $v = 0$ corresponds to $A^+ {}^2\Sigma_u^+$, the other levels to $X^+ {}^2\Sigma_g^+$.

v	$\tau_{\text{eff}}(293 \text{ K}) \text{ (s)}$			
	$N = 0$	1	2	3
0	1.0620[−01]	1.2558[−01]	1.8600[−01]	
19	3.1955[−01]	5.2335[−01]		
18	1.7810[−02]	1.9270[−02]	2.2940[−02]	3.2010[−02]
17	4.4200[−03]	4.4800[−03]	4.6400[−03]	4.9300[−03]
16	6.5200[−03]	6.3200[−03]	5.9600[−03]	5.4900[−03]
15	5.1070[−02]	4.7850[−02]	4.2070[−02]	3.4890[−02]

Note: Table entries $a[b]$ stand for $a \times 10^b$.

(ii) Using adiabatic wave functions and energies leads to $\Delta A/A = 0.0104$ and $\Delta \tau_{\text{eff}}/\tau_{\text{eff}} = 0.0012$. (iii) Using adiabatic wave functions and nonadiabatic energies including relativistic and radiative corrections from Ref. [24], but increasing the stepsize of the potential to $0.02a_0$, we obtain $\Delta A/A = 0.0002$ and $\Delta \tau_{\text{eff}}/\tau_{\text{eff}} = 0.0016$.

4. Discussion and outlook

This work sought to calculate the rovibronic population redistribution induced by BBR to determine the viability of conducting microwave spectroscopy of the weakly

Table 2. Effective lifetimes of the weakly bound states of H_2^+ at 77 K. Level $v = 0$ corresponds to $\text{A}^+ \ ^2\Sigma_u^+$, the other levels to $\text{X}^+ \ ^2\Sigma_g^+$.

v	$\tau_{\text{eff}}(77 \text{ K}) \text{ (s)}$			
	$N = 0$	1	2	3
0	1.9700[−01]	2.3700[−01]	3.7400[−01]	
19	5.1190[+00]	8.3910[+00]		
18	3.6300[−01]	4.0900[−01]	5.2000[−01]	8.0700[−01]
17	3.2600[−01]	3.0300[−01]	2.6100[−01]	2.1600[−01]
16	5.8191[+01]	4.8358[+01]	3.3474[+01]	1.9685[+01]
15	8.9116[+04]	1.9420[+05]	3.3290[+05]	4.3669[+05]

Note: Table entries $a[b]$ stand for $a \times 10^b$.

bound states of state-selectively produced, trapped H_2^+ ions. The necessity to include the effect of BBR for estimating effective lifetimes is motivated by the overlap of the BBR spectrum at room temperature with the $\text{A}^+ \ ^2\Sigma_u^+ - \text{X}^+ \ ^2\Sigma_g^+$ electronic spectrum of H_2^+ .

We presented the time evolution of the internal state distribution for room temperature and liquid nitrogen temperature. Interestingly, it was found that the largest contribution to the population redistribution comes from absorption to the continuum, given by \bar{B}_{cont} . These coefficients are one to two orders of magnitude larger than A and \bar{B} at 293 K, and of the same order of magnitude at 77 K. The rovibrational level with the largest photodissociation rate is $\text{X}^+(17, 0)$ with $\bar{B}_{\text{cont}} = 224.504 \text{ s}^{-1}$ at 293 K and, in contrast, $A = 0.715 \text{ s}^{-1}$ and $\bar{B} = 0.638 \text{ s}^{-1}$ for $\text{A}^+(0, 1) \rightarrow \text{X}^+(17, 0)$.

As the main result of this work, we find effective lifetimes of the order of milliseconds at 293 K, which can be increased to hundreds of milliseconds or even seconds at 77 K. This finding is in agreement with the measurements reported in Refs. [8,9,11,44], which demonstrated the possibility of conducting molecular ion-beam experiments in the microwave range with an interaction time of 0.3 μs .

More importantly, the found lifetimes of the highly excited, weakly bound states will allow for state-of-the-art ion trap experiments with millisecond interaction times, similar to the ones carried out using the vibrational ground state in HD^+ . Specifically, the lifetimes are sufficiently long to enable transport and trap-loading of the ions, prepared in a separate photoexcitation region. The $\text{X}^+(v = 19)$ levels are identified as optimal ‘transfer states’ by having the longest lifetimes among the weakly bound states at room and liquid nitrogen temperature. Once the ions are moved into the trap, the population could be transferred to different science states by adiabatic passage using microwave radiation. We also determined effective lifetimes at 400 K, which are shown in Figure 5 and listed in Table 3, for the case of elevated temperatures in the trap region, which might be caused by rf heating. Compared

Table 3. Effective lifetimes of the weakly bound states of H_2^+ at 400 K. Level $v = 0$ corresponds to $\text{A}^+ \ ^2\Sigma_u^+$, the other levels to $\text{X}^+ \ ^2\Sigma_g^+$.

v	$\tau_{\text{eff}}(400 \text{ K}) \text{ (s)}$			
	$N = 0$	1	2	3
0	8.4630[−02]	9.9690[−02]	1.4399[−01]	
19	1.5871[−01]	2.6052[−01]		
18	8.7600[−03]	9.4600[−03]	1.1230[−02]	1.5650[−02]
17	2.1500[−03]	2.2000[−03]	2.2900[−03]	2.4600[−03]
16	2.0500[−03]	2.0200[−03]	1.9600[−03]	1.8900[−03]
15	7.1100[−03]	6.8100[−03]	6.2700[−03]	5.5500[−03]

Note: Table entries $a[b]$ stand for $a \times 10^b$.

to room temperature, the lifetimes are reduced by about a factor of two.

The effect of g/u -mixing experienced mainly by the $\text{X}^+(19, 0)$ and $\text{X}^+(19, 1)$ levels was found to reduce their fluorescence lifetime by 30% to about 1000 s [45]. In this work, we found that the effect of g/u -mixing is negligible when the interaction with BBR is included: the effective lifetime of $\text{X}^+(19, 1)$ is reduced by only 210 μs , about 0.011%, and the effective lifetime of $\text{X}^+(19, 0)$ is reduced by merely 60 μs , about 0.001%.

Other compelling findings of this study are the following: (i) The lifetime of $\text{A}^+(0)$ does not significantly vary with temperature and barely doubles when going from 293 to 77 K. This is because the state has a vanishing PDCS well before the peak of the BBS and the contribution from dissociation mostly comes from the GHz region, where the BBS does not decrease as drastically with temperature as in the THz region (see Figure 2). This may set a limit on the interaction time of experiments relying on this state; (ii) The states of $\text{X}^+(\leq 18)$ cannot decay via electric-dipole transitions and their lifetime from electric-quadrupole transitions are on the order of days, nonetheless, as a consequence of BBR, they have an effective lifetime even shorter than the higher vibrational levels; (iii) For an initial population of 10^3 ions in $\text{X}^+(19)$ levels (see Figure 3), only one ion is expected to reach $\text{A}^+(0)$ by the time this state reaches its maximum population, while most of the total population is transferred to the continuum. This means, that the high purity of state-selectively prepared molecular ion ensembles is conserved, enabling a high signal-to-noise ratio.

Experiments with trapped H_2^+ ions relying on weaker two-photon or electric-quadrupole transitions can make use of more strongly bound X^+ states, for which BBR-induced photodissociation is irrelevant. Several such studies are currently pursued, in one case H_2^+ ions are produced in the vibrational ground state $\text{X}^+(v = 0, N)$ by photoionisation inside a rf trap [46], whereas in the other case a single H_2^+ ion is injected into a Penning trap,

which allows to determine the rovibrational state before driving a spectroscopic transition [47].



Disclosure statement

No potential conflict of interest was reported by the author(s).

Funding

MB acknowledges NWO for a VENI grant (VI.Veni.202.140).

ORCID

A. D. Ochoa Franco  <http://orcid.org/0000-0002-0313-662X>
M. Beyer  <http://orcid.org/0000-0003-0053-9666>

References

- [1] S. Alighanbari, G.S. Giri, F.L. Constantin, V.I. Korobov and S. Schiller, *Nature* **581**, 152–158 (2020). doi:10.1038/s41586-020-2261-5
- [2] S. Patra, M. Germann, J.-P. Karr, M. Haidar, L. Hilico, V.I. Korobov, F.M.J. Cozijn, K.S.E. Eikema, W. Ubachs and J.C.J. Koelemeij, *Science* **369**, 1238–1241 (2020). doi:10.1126/science.aba0453
- [3] V.I. Korobov, L. Hilico and J.-P. Karr, *Phys. Rev. A* **89**, 032511 (2014). doi:10.1103/PhysRevA.89.032511
- [4] V.I. Korobov, L. Hilico and J.-P. Karr, *Phys. Rev. Lett.* **118**, 233001 (2017). doi:10.1103/PhysRevLett.118.233001
- [5] J.C.J. Koelemeij, B. Roth, A. Wicht, I. Ernsting and S. Schiller, *Phys. Rev. Lett.* **98**, 173002 (2007). doi:10.1103/PhysRevLett.98.173002
- [6] P. Bunker, *Chem. Phys. Lett.* **27**, 322–324 (1974). doi:10.1016/0009-2614(74)90233-4
- [7] J.M. Peek, A. Hashemi-Attar and C.L. Beckel, *J. Chem. Phys.* **71**, 5382 (1979). doi:10.1063/1.438353
- [8] A. Carrington, I.R. McNab and C.A. Montgomerie, *Chem. Phys. Lett.* **160**, 237–242 (1989). doi:10.1016/0009-2614(89)87589-X
- [9] A. Carrington, I.R. McNab, C.A. Montgomerie and J.M. Brown, *Mol. Phys.* **66**, 1279–1289 (1989). doi:10.1080/00268978900100881
- [10] A. Carrington, C.A. Leach, R.E. Moss, T.C. Steimle, M.R. Viant and Y.D. West, *J. Chem. Soc. Faraday Trans.* **89**, 603 (1993). doi:10.1039/ft9938900603
- [11] A. Carrington, C.A. Leach, A.J. Marr, R.E. Moss, C.H. Pyne and T.C. Steimle, *J. Chem. Phys.* **98**, 5290–5301 (1993). doi:10.1063/1.464928
- [12] A. Carrington, C.A. Leach and M.R. Viant, *Chem. Phys. Lett.* **206**, 77–82 (1993). doi:10.1016/0009-2614(93)85520-X
- [13] L. Augustovićová, P. Soldán, W.P. Kraemer and V. Špirko, *MNRAS* **439**, 1136–1139 (2014). doi:10.1093/mnras/stu060
- [14] S.C. Menasian, Ph.D. thesis, School University of Washington, Seattle, 1973.
- [15] L. Zhu and P. Johnson, *J. Chem. Phys.* **94**, 5769–5771 (1991). doi:10.1063/1.460460
- [16] S. Mackenzie and T. Softley, *J. Chem. Phys.* **101**, 10609–10617 (1994). doi:10.1063/1.467875
- [17] M. Beyer and F. Merkt, *Phys. Rev. Lett.* **116**, 093001 (2016). doi:10.1103/PhysRevLett.116.093001
- [18] M. Beyer and F. Merkt, *Phys. Rev. X* **8**, 031085 (2018). doi:10.1103/PhysRevX.8.031085
- [19] M. Beyer and F. Merkt, *Mol. Phys.* e2048108 (2022). doi:10.1080/00268976.2022.2048108
- [20] E. Reinhold, W. Hogervorst and W. Ubachs, *Phys. Rev. Lett.* **78**, 2543–2546 (1997). doi:10.1103/PhysRevLett.78.2543
- [21] E. Reinhold, W. Hogervorst, W. Ubachs and L. Wolniewicz, *Phys. Rev. A* **60**, 1258–1270 (1999). doi:10.1103/PhysRevA.60.1258
- [22] A. de Lange, W. Hogervorst, W. Ubachs and L. Wolniewicz, *Phys. Rev. Lett.* **86**, 2988–2991 (2001). doi:10.1103/PhysRevLett.86.2988
- [23] E. Reinhold and W. Ubachs, *Mol. Phys.* **103**, 1329–1352 (2005). doi:10.1080/00268970500050621
- [24] R.E. Moss, *Mol. Phys.* **80**, 1541–1554 (1993). doi:10.1080/00268979300103211
- [25] P.R. Bunker and R.E. Moss, *Chem. Phys. Lett.* **316**, 266–270 (2000). doi:10.1016/S0009-2614(99)01301-9
- [26] M. Beyer and F. Merkt, *J. Mol. Spectrosc.* **330**, 147–157 (2016). doi:10.1016/j.jms.2016.08.001
- [27] E. Tiesinga, P.J. Mohr, D.B. Newell and B.N. Taylor, *J. Phys. Chem. Ref. Data* **50**, 033105 (2021). doi:10.1063/5.0064853
- [28] B.R. Johnson, *J. Chem. Phys.* **67**, 4086 (1977). doi:10.1063/1.435384
- [29] J. Carbonell, R. Lazauskas, D. Delande, L. Hilico and S. Kiliç, *Europhys. Lett.* **64**, 316 (2003). doi:10.1209/epl/i2003-00176-1
- [30] E. Merzbacher, *Quantum Mechanics* (Jones & Bartlett Publishers, 1961).
- [31] M. Beyer and F. Merkt, *J. Chem. Phys.* **149**, 214301 (2018). doi:10.1063/1.5046147
- [32] M. Larsson, *Astron. Astrophys.* **128**, 291 (1983).
- [33] J.M. Brown and A. Carrington, *Rotational Spectroscopy of Diatomic Molecules* (Cambridge University Press, 2003).
- [34] R.N. Zare, *Angular Momentum: Understanding Spatial Aspects in Chemistry and Physics* (John Wiley & Sons, New York, 1988).
- [35] J.K. Watson, *J. Mol. Spectrosc.* **252**, 5–8 (2008). doi:10.1016/j.jms.2008.04.014
- [36] H. Lefebvre-Brion and R.W. Field, *The Spectra and Dynamics of Diatomic Molecules: Revised and Enlarged Edition* (Elsevier, 2004).
- [37] E.E. Whiting, Ph.D. thesis, School York University, Ontario, 1972.
- [38] A. Thorne, *Spectrophysics* (Chapman and Hall, 1974).
- [39] J. Koelemeij, *Phys. Chem. Chem. Phys.* **13**, 18844 (2011). doi:10.1039/c1cp21204d
- [40] M.H. Howells and R.A. Kennedy, *Chem. Phys. Lett.* **184**, 521–525 (1991). doi:10.1016/0009-2614(91)80028-V
- [41] R.S. Mulliken, *J. Chem. Phys.* **7**, 20–34 (1939). doi:10.1063/1.1750319
- [42] A.D.J. Critchley, A.N. Hughes and I.R. McNab, *Phys. Rev. Lett.* **86**, 1725–1728 (2001). doi:10.1103/PhysRevLett.86.1725
- [43] W. Demtröder, *Laser Spectroscopy 1: Basic Principles* (Springer, 2014).
- [44] A. Carrington, *Science* **274**, 1327–1331 (1996). doi:10.1126/science.274.5291.1327

- [45] R.E. Moss, Chem. Phys. Lett. **206**, 83–90 (1993). doi:10.1016/0009-2614(93)85521-O
- [46] J. Schmidt, T. Louvradoux, J. Heinrich, N. Sillitoe, M. Simpson, J.-P. Karr and L. Hilico, Phys. Rev. Appl. **14**, 024053 (2020). doi:10.1103/PhysRevApplied.14.024053
- [47] B. Tu, F. Hahne, I. Arapoglou, A. Egl, F. Heiße, M. Höcker, C. König, J. Morgner, T. Sailer, A. Weigel, R. Wolf and S. Sturm, Adv. Quantum Technol. **4**, 2100029 (2021). doi:10.1002/qute.v4.72104.03719.

Appendices

Appendix 1. Coupling constant for the Fermi contact interaction

The Fermi coupling constants of the weakly bound states were obtained by averaging the electron density at the position of the nuclei using the rovibrational wave functions obtained in Section 2.1, that is,

$$b_F(\eta, v, N) = \frac{8\pi}{3} \frac{g_s g_p \mu_B \mu_N}{4\pi \epsilon_0 c^2} \langle \eta v N | \rho_e(R) | \eta v N \rangle, \quad (\text{A1})$$

where

$$\rho_e(R) = \langle \eta | \delta(\mathbf{r} - \mathbf{R}) | \eta \rangle, \quad (\text{A2})$$

which was taken from Ref. [18], and η indicating the electronic state. The results are listed in Tables A1 and A2.

Appendix 2. Numerical results from the electric-dipole moment

The numerical results for the bound-bound line strengths and the Einstein rate coefficients computed in Section 2 are summarised in Tables A3–A5. Absorption rate coefficients for the excitation into the continuum are presented in Tables A6 and A7.

Table A1. Effective coupling constants of the Fermi interaction for the weakly bound states of H_2^+ in $X^+ \ ^2\Sigma_g^+$.

v	b_F (MHz)	
	$N = 1$	3
13	728.41	726.70
14	722.46	721.02
15	717.73	716.58
16	714.25	713.41
17	712.07	711.58
18	711.27	711.17
19	711.38	

Table A2. Effective coupling constants of the Fermi interaction for the weakly bound states of H_2^+ in $A^+ \ ^2\Sigma_u^+$.

v	b_F (MHz)	
	$N = 0$	2
0	711.32	711.32

Table A3. Bound-bound line strengths and Einstein rate coefficients of the weakly bound states of H_2^+ for transitions involving $\text{A}^+ (0, 1)$.

$\text{A}^+ \ ^2\Sigma_u^+ v = 0, N = 1$							
v	N	ν (THz)	μ_e (ea_0)	S ($e^2a_0^2$)	A (s^{-1})	\bar{B} (s^{-1})	
*19	0	5.2890[−02]	7.8405[+00]	1.2295[+02]	6.8403[−04]	7.8613[−02]	2.0409[−02]
18	2	3.5197[−01]	4.7023[+00]	8.8448[+01]	4.8334[−02]	8.1445[−01]	1.9704[−01]
18	0	6.4562[−01]	3.7955[+00]	2.8812[+01]	9.7175[−02]	8.7118[−01]	1.9615[−01]
17	2	3.8904[+00]	6.4155[−01]	1.6463[+00]	1.2150[+00]	1.3632[+00]	1.1796[−01]
17	0	4.5903[+00]	5.4325[−01]	5.9025[−01]	7.1549[−01]	6.3828[−01]	4.3417[−02]
16	2	1.1809[+01]	9.7880[−02]	3.8320[−02]	7.9082[−01]	1.3361[−01]	5.0338[−04]
16	0	1.2872[+01]	8.5060[−02]	1.4470[−02]	3.8679[−01]	5.3463[−02]	1.2688[−04]
15	2	2.3980[+01]	1.6470[−02]	1.0900[−03]	1.8762[−01]	3.7676[−03]	6.0557[−08]
15	0	2.5368[+01]	1.4500[−02]	4.2000[−04]	8.6064[−02]	1.3712[−03]	1.1694[−08]

Note: Rate coefficients for absorption can be obtained using the tabulated values and Equation (21). The first and second column of \bar{B} present the values at 293 and 77 K, respectively. * Level X^+ (19) lies above $\text{A}^+ (0)$ and thus the rate coefficients, A and B , reported in this row take the former as the upper state. $a[b]$ stands for $a \times 10^b$.

Table A4. Bound-bound line strengths and Einstein rate coefficients of the weakly bound states of H_2^+ for transitions involving $\text{A}^+ (0, 2)$.

$\text{A}^+ \ ^2\Sigma_u^+ v = 0, N = 2$							
v	N	ν (THz)	μ_e (ea_0)	S ($e^2a_0^2$)	A (s^{-1})	\bar{B} (s^{-1})	
*19	1	1.7610[−02]	9.1888[+00]	3.3774[+02]	2.3115[−02]	8.0022[+00]	2.0945[+00]
18	3	1.5664[−01]	5.5070[+00]	1.8196[+02]	5.2584[+00]	2.0234[+02]	5.1276[+01]
18	1	5.9369[−01]	3.5779[+00]	5.1205[+01]	8.0575[+01]	7.8894[+02]	1.7994[+02]
17	3	3.2774[+00]	6.2199[−01]	2.3212[+00]	6.1447[+02]	8.6476[+02]	9.1554[+01]
17	1	4.4040[+00]	4.6558[−01]	8.6704[−01]	5.5692[+02]	5.2677[+02]	3.8241[+01]
16	3	1.0827[+01]	8.9435[−02]	4.7992[−02]	4.5809[+02]	9.3651[+01]	5.3778[−01]
16	1	1.2565[+01]	7.0481[−02]	1.9870[−02]	2.9641[+02]	4.3391[+01]	1.1773[−01]
15	3	2.2672[+01]	1.4634[−02]	1.2849[−03]	1.1260[+02]	2.8149[+00]	8.2142[−05]
15	1	2.4953[+01]	1.1808[−02]	5.5775[−04]	6.5168[+01]	1.1125[+00]	1.1468[−05]

Note: See caption of Table A3 for details. Line strengths are given for states with $G = 1/2$; the corresponding value for states with $G = 3/2$ can be obtained according to Equation (11) and are twice as large. $a[b]$ stands for $a \times 10^b$.

Table A5. Bound-bound line strengths and Einstein rate coefficients of the weakly bound states of H_2^+ for transitions involving $\text{A}^+ (0, 0)$.

$\text{A}^+ \ ^2\Sigma_u^+ v = 0, N = 0$							
v	N	ν (THz)	μ_e (ea_0)	S ($e^2a_0^2$)	A (s^{-1})	\bar{B} (s^{-1})	
*19	1	9.6431[−02]	6.2200[+00]	7.7376[+01]	8.6959[−01]	5.4620[+01]	1.4038[+01]
18	1	5.1487[−01]	4.2445[+00]	3.6032[+01]	1.8491[+02]	2.1014[+03]	4.8869[+02]
17	1	4.3252[+00]	6.2061[−01]	7.7032[−01]	2.3435[+03]	2.2734[+03]	1.6960[+02]
16	1	1.2486[+01]	9.7541[−02]	1.9029[−02]	1.3927[+03]	2.0692[+02]	5.8105[−01]
15	1	2.4875[+01]	1.6667[−02]	5.5558[−04]	3.2150[+02]	5.5611[+00]	5.9428[−05]

Note: See caption of Table A3 for details. Line strengths are given for states with $G = 1/2$; the corresponding value for states with $G = 3/2$ can be obtained according to Equation (11) and are twice as large. $a[b]$ stands for $a \times 10^b$.

Table A6. Continuum absorption rates of the weakly bound states of H_2^+ at 293 K.

$\bar{B}_{\text{cont}}(293 \text{ K}) (s^{-1})$				
v	$N = 0$	1	2	3
0	4.1756[−01]	5.6180[−01]	6.6154[−01]	
19	3.0503[+00]	1.8482[+00]		
18	5.3561[+01]	4.9919[+01]	4.3118[+01]	3.1106[+01]
17	2.2450[+02]	2.2149[+02]	2.1496[+02]	2.0232[+02]
16	1.5328[+02]	1.5815[+02]	1.6787[+02]	1.8211[+02]
15	1.9577[+01]	2.0902[+01]	2.3772[+01]	2.8667[+01]

Note: $a[b]$ stands for $a \times 10^b$.

Table A7. Continuum absorption rates of the weakly bound states of H_2^+ at 77 K.

v	$\bar{B}_{\text{cont}}(77 \text{ K}) (\text{s}^{-1})$			
	$N = 0$	1	2	3
0	9.7873[−02]	1.3250[−01]	1.2351[−01]	
19	1.7430[−01]	1.0228[−01]		
18	2.1915[+00]	2.0166[+00]	1.8094[+00]	1.2036[+00]
17	2.9510[+00]	3.2089[+00]	3.7731[+00]	4.5669[+00]
16	1.6840[−02]	2.0366[−02]	2.9630[−02]	5.0481[−02]
15	2.3250[−06]	3.0429[−06]	5.1857[−06]	1.1280[−05]

Note: $a[b]$ stands for $a \times 10^b$.